



OPEN Molecular dynamics simulation of atomic layer etching for sidewall damage recovery in GaN-based structures

Eun Koo Kim^{1,2,9}, Jong Woo Hong^{3,9}, Woong Sun Lim⁴, Ja Yeon Kim⁵, Kyung Lim Kim^{1,2}, Jong Soon Park^{1,2}, Yun Jae Park^{1,2}, Chan Ho Kim⁶, Hyeong Joon Eoh⁶, Jun Won Jeong⁷, Sung Hyun Kim⁶, Young Woo Jeon⁸, Dong Woo Kim³ & Geun Young Yeom^{3,6}✉

Today, as GaN-based devices are becoming increasingly smaller, dry etching has been employed, but it has caused damage, particularly in InGaN/GaN multiple quantum well (MQW) structures exposed to Cl₂-based reactive ion etching (RIE). Attempts to remove this damage with wet etching have had limitations. Therefore, atomic layer etching (ALE) has emerged as a promising technique to overcome the sidewall damage issues in GaN-based devices. This study utilized molecular dynamics (MD) simulations to investigate the optimal ALE process conditions for recovering plasma-induced damage at the atomic scale. The simulations systematically analyzed the effect of the Ar⁺ ion incidence angle on etching behavior and recovery efficiency. Three surfaces with initial damage conditions high, middle, and low were generated and then subjected to the ALE process. As a result, the ALE process was found to effectively remove both surface and subsurface amorphized regions, with more than ~47% reduction in damaged atoms observed across all damage levels, and ultimately converging to a comparable level of residual surface damage. Furthermore, a dual-angle approach using 60°–70° for deep damage removal followed by 80° for surface smoothing was identified as the most effective strategy for maximizing recovery while minimizing roughness. These findings highlight the strong potential of ALE to fundamentally recover MQW sidewall damage regardless of the initial damage level, while also providing critical physical insights and practical guidelines for optimizing the manufacturing processes of next-generation vertical GaN-based devices.

Keywords GaN, InGaN, Simulation, Molecular dynamics, MQW, Atomic layer etching

GaN has a wide bandgap and high electron mobility, making it suitable for use in light emitting diodes (LEDs) and power devices.^{1–3} These inorganic-based devices also boast outstanding brightness, energy efficiency, and a long lifespan, which fulfills the core requirements of future technology platforms like augmented reality (AR), virtual reality (VR), ultra-high-resolution displays, and wearable devices.^{4–9} While wet etching with solutions like Potassium Hydroxide (KOH) and Tetramethylammonium hydroxide (TMAH) can be used for GaN fabrication, dry etching using reactive ion etching (RIE) is generally employed for smaller devices and higher throughput.^{10–12}

However, the mesa etching process, which is essential for defining individual pixels, is cited as one of the biggest obstacles to the commercialization of GaN-based devices.^{13–15} In particular, the Cl₂-based RIE process, widely used for its high patterning precision, causes severe physical and chemical damage to the multiple

¹Department of Semiconductor and Display Engineering, Sungkyunkwan University (SKKU), Suwon 16419, Gyeonggi-do, Republic of Korea. ²Samsung Institute of Technology, Samsung-ro 1, Giheung-gu, Yongin-si 17113, Gyeonggi-do, Republic of Korea. ³School of Advanced Materials Science and Engineering, Sungkyunkwan University (SKKU), Suwon 16419, Gyeonggi-do, Republic of Korea. ⁴Korea Advanced Nano Fab Center (KANC), Suwon 16229, Gyeonggi-do, Republic of Korea. ⁵Korea Photonics Technology Institute (KOPTI), Gwangju 500-460, Republic of Korea. ⁶SKKU Advanced Institute of Nanotechnology (SAINT), Sungkyunkwan University (SKKU), Suwon 16419, Gyeonggi-do, Republic of Korea. ⁷Department of Semiconductor Convergence Engineering, Sungkyunkwan University (SKKU), Suwon 16419, Gyeonggi-do, Republic of Korea. ⁸Department of Display Engineering, Sungkyunkwan University (SKKU), Suwon 16419, Gyeonggi-do, Republic of Korea. ⁹Eun Koo Kim, Jong Woo Hong, these authors contributed equally. ✉email: gyeom@skku.edu

quantum well (MQW) sidewalls due to high-energy ion bombardment and reactive plasma.^{16–19} To recover from etch damage, post-RIE treatments like wet etching using KOH and TMAH have been used, but they have not been very effective.^{20–22}

An alternative that is emerging to overcome the limitations of recovering from this etch damage is atomic layer etching (ALE) technology.^{23,24} ALE can be classified into isotropic and anisotropic types depending on the directionality of ion bombardment and etching reactions. Isotropic ALE, which has been extensively studied in previous works, enables uniform etching in all directions and is typically applied to planar surfaces. In contrast, anisotropic ALE utilizes directionally controlled etching, which is essential for vertical device architectures. In this study, we focus on anisotropic ALE, where a controlled ion incidence angle is employed to achieve vertical sidewall damage recovery in GaN-based MQW structures.^{10,25–27} The core of this technology is the temporal separation of the chemical reaction and physical removal, allowing for precise control over each step, unlike the chaotic simultaneous reactions of the RIE process.²⁸ Using ALE, it is possible to precisely and surgically remove only the damaged atomic layers while minimizing additional damage.^{10,29} This process reveals a surface with atomic-level flatness and a perfect crystal structure.^{29,30} Recently, experimental results applying the ALE process to the sidewalls of μ LEDs have been reported, showing improvements in photoluminescence (PL), which proves the potential of this technology as a next-generation solution for the sidewall damage problem.³¹

However, as next-generation processes demand the verticality of GaN-based devices, damage recovery on vertical structures is necessary after RIE. In conventional ALE processes, ions are incident nearly perpendicular to the wafer surface, making it difficult to effectively transfer energy to the vertical MQW sidewalls. To address this issue, equipment capable of precisely controlling the ion incidence angle by adjusting the substrate tilt, such as an ion beam etching (IBE) system, is essential.^{32,33} Consequently, the ion incidence angle is the most critical parameter in determining the efficiency of damaged layer removal and the quality of the final surface. While some studies have investigated the importance of the angle in GaN etching, no research has systematically elucidated the effect of the ion incidence angle for recovering and optimizing ion damage to the complex, multilayered MQW sidewalls.

This study aims to address this critical research gap. Utilizing a molecular dynamics (MD) simulation technique, we will systematically analyze the effect of varying Ar^+ ion incidence angles on the ALE-based recovery process of plasma-damaged MQW(InGaN/GaN) sidewalls at the atomic level.^{34,35} By quantitatively evaluating the removal rate of damaged atoms, the degree of crystal structure restoration, and the changes in surface roughness under various ion incidence angle conditions, we will elucidate the optimal ALE process conditions for sidewall damage recovery. The results of this work are expected to provide fundamental physical insights and practical process design guidelines necessary for minimizing non-radiative losses and maximizing the quantum efficiency of GaN-based devices, thereby contributing to the accelerated commercialization of next-generation display technologies.

Methodology

Simulation structures

The MD simulations in this study were performed using the Large-scale Atomic/Molecular Massively Parallel Simulator (LAMMPS). The simulation models employed three initial structures shown in Figure 1 (a–c) for GaN, $\text{In}_{0.2}\text{Ga}_{0.8}\text{N}$, and a GaN(30 Å)/ $\text{In}_{0.2}\text{Ga}_{0.8}\text{N}$ (40 Å) MQW structure, respectively. The c-plane ([0001] surface) of the structure was set to be aligned along the z-axis, and the a-plane ([1–100] surface), which represents the sidewall where ions are incident, was aligned along the y-axis. To independently analyze the damage caused by the etching process, the initial models were constructed as ideal, defect-free crystal structures, excluding intrinsic defects that might occur during crystal growth. In addition, periodic boundary conditions were applied along the x- and z- directions to represent the extended nature of the crystal lattice. The bottommost 5 Å was defined as a fixed layer with fixed atom positions. 20 Å thermostat layer was then established on the top of the fixed layer, where a Langevin thermostat was applied to serve as a heat sink, mimicking the dissipation of thermal energy from ion collisions into the bulk substrate. The remaining upper portion, where actual etching reactions occur, was configured as a Newtonian layer, following Newtonian dynamics without artificial control.

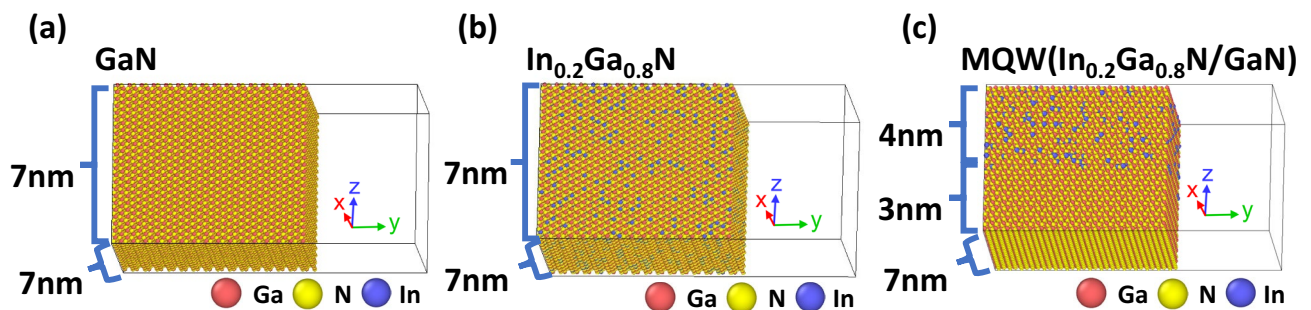


Fig. 1. Three initial structures used for simulation models: (a) GaN, (b) $\text{In}_{0.2}\text{Ga}_{0.8}\text{N}$, and (c) an MQW ($\text{In}_{0.2}\text{Ga}_{0.8}\text{N}/\text{GaN}$).

Interatomic potentials

The interatomic interactions used in the simulations were described through the hybrid potential function of LAMMPS, which combined Stillinger-Weber, Ziegler-Biersack-Littmark, and Lennard-Jones potentials depending on the type of interaction.^{36–39}

Stillinger-Weber (SW) potential

The many-body interactions between Ga, In, N, and Cl atoms were described using the Stillinger-Weber (SW) potential.^{40,41} The SW potential is composed of a sum of two-body and three-body terms, and its form is as follows:

$$E_{SW} = \sum_{i < j} v_2(r_{ij}) + \sum_{i < j < k} v_3(r_{ij}, r_{ik}, \theta_{ijk})$$

$$v_2(r_{ij}) = A \cdot \varepsilon \cdot \left[B \cdot \left(\frac{\sigma}{r_{ij}} \right)^p - \left(\frac{\sigma}{r_{ij}} \right)^q \right] \cdot \exp \left(\frac{\sigma}{r_{ij} - a \cdot \sigma} \right)$$

$$v_3(r_{ij}, r_{ik}, \theta_{ijk}) = \lambda \cdot \varepsilon \cdot (\cos \theta_{ijk} - \cos \theta_0)^2 \cdot \exp \left[\frac{\gamma \sigma}{r_{ij} - a \cdot \sigma} + \frac{\gamma \sigma}{r_{ik} - a \cdot \sigma} \right]$$

The potential employed in this study, originally developed by X. W. Zhou et al.⁴², was optimized to yield the lowest energy for both wurtzite and zinc-blende structures of GaN and InN. This potential has undergone rigorous validation, accurately reproducing key physical properties such as atomic volume, cohesive energy, and bulk modulus measured in actual experiments. Furthermore, it has demonstrated stable crystal growth in deposition simulations using molecular dynamics, confirming its reliability. Therefore, this potential can be considered as a robust model capable of reliably simulating the dynamic phenomena of GaN-based materials.

Parameters for describing the Cl-substrate (Ga, In, N) interactions were newly developed for this study. Figure 2 (a–d) presents the corresponding two-body term force fitting data. The new parameters were determined by fitting data obtained through density functional theory (DFT) calculations using the Quantum Espresso. These DFT calculations utilized the Perdew-Burke-Ernzerhof (PBE) exchange-correlation functional and Projector Augmented-Wave (PAW) pseudopotentials. While the three-body angular term of the SW potential was fitted, the λ and γ parameters were mostly kept constant at 32.5 and 12.5, respectively, since these values were also fixed in the existing In–Ga–N potential. This approach was adopted to preserve consistency with the established parameterization and ensure compatibility across the potential set. (See the supplementary information Table S1, Table S2)

Ziegler-Biersack-Littmark (ZBL) potential

The high-energy collision phenomena between Ar⁺ ions and other atoms (Ga, In, N, Cl) were described using the Ziegler-Biersack-Littmark (ZBL) screened Coulomb potential.^{43,44} The form of the ZBL potential is as follows.

$$V_{ZBL}(r) = \frac{1}{4\pi\epsilon_0} \frac{Z_1 Z_2 e^2}{r} \phi! \left(\frac{r}{a} \right)$$

This potential effectively models the strong repulsive forces that arise at very short interatomic distances and is thus employed to accurately represent physical sputtering phenomena.

Lennard-Jones (LJ) potential

The interactions between Ar⁺ ions were described using the Lennard-Jones (LJ) potential.^{45–47} This potential was chosen because Argon, as a noble gas, is spherically symmetric and electrically neutral. Consequently, the interactions between Ar⁺ ions are well-described by the short-range attractive (van der Waals) and repulsive (Pauli repulsion) forces that the Lennard-Jones potential effectively models. And incident Ar⁺ ions were assumed to be neutralized through the Auger effect near the surface and were therefore modeled as neutral Ar atoms in the simulations. The form of the LJ potential is given as follows.

$$V_{LJ}(r) = 4\epsilon \left[\left(\frac{\sigma}{r} \right)^{12} - \left(\frac{\sigma}{r} \right)^6 \right]$$

The LJ parameters used in this simulation ($\epsilon = 0.0103$ eV, $\sigma = 3.4$ Å) were adopted from the study by Sun et al.⁴⁸

Molecular dynamics procedure

Prior to the main simulations, the etch amount per cycles (EPCs) of the ALE process for blanket GaN and In_{0.2}Ga_{0.8}N structures were calibrated to match the experimental values reported in a previous study from our laboratory, as shown in Figure 3 (a). The Ar⁺ ion energy was set to 50 eV, representing the nominal incident energy used in the simulations without considering the additional plasma potential. In practical plasma systems, the actual ion energy may be slightly higher due to the plasma potential, but this difference does not affect the comparative trends discussed in this study. In this calibration step, not only the Ar⁺ ion parameters but also the removal rate of volatile byproducts such as GaCl₃ and N₂ during the desorption stage was adjusted, ensuring that the resulting EPC values matched with the experimental measurements. Based on this calibration, simulation parameters were established to reproduce EPC values of ~2.4 Å/cycle for GaN and ~2.9 Å/cycle for

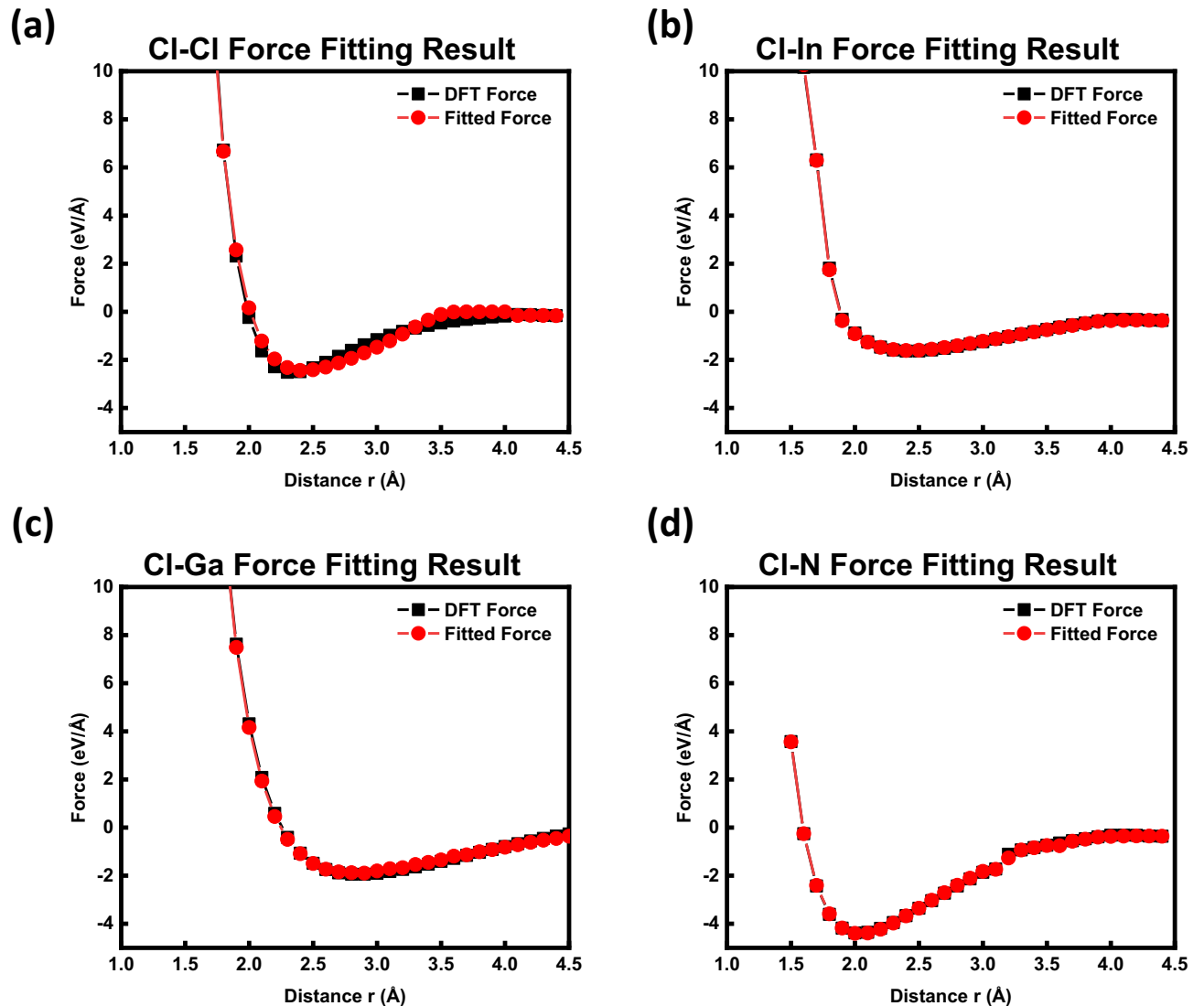


Fig. 2. Force fitting data developed for simulation of (a) Cl–Cl, (b) Cl–In, (c) Cl–Ga, and (d) Cl–N interactions.

$\text{In}_{0.2}\text{Ga}_{0.8}\text{N}$ structures. The key process parameters determined during this calibration include a chemisorption duration of 7.5 ps, an Ar^+ ion energy of 50 eV during the desorption step, and a dose of 350 Ar^+ ions per cycle. These parameters were consistently applied in all subsequent simulations of the MQW structures.^{10,25} Moreover, to enhance the robustness of model validation beyond EPC alone, we compared our simulation results with literature-reported experimental trends in atomic layer etching. Specifically, the evolution of surface roughness, the decrease in amorphous atom counts, and the angle-dependent behavior of damage recovery showed qualitative agreement with findings in previous experimental ALE studies on GaN and InGaN. Although exact quantitative comparisons are limited by the lack of atomic-scale experimental resolution, the observed trend similarities support the physical validity and process relevance of the simulation framework. Figure 3(b) illustrates the etching depth per cycle for GaN and $\text{In}_{0.2}\text{Ga}_{0.8}\text{N}$ at an ion incidence angle of 80° . The ion incidence angle was defined as the angle measured from the sample surface, such that normal incidence corresponds to 0° .

Subsequently, to evaluate the damage recovery capability of the ALE process, three types of initially damaged surfaces, which are generally formed during mesa etching using RIE, were prepared by irradiating with Ar^+ ion beams under different conditions. As summarized in Table 1, a high damage surface was generated by irradiating 5,000 Ar^+ ions with 1,000 eV, a middle damage surface by irradiating 800 Ar^+ ions with 700 eV and a low damage surface by irradiating 2,000 Ar^+ ions with 300 eV, with the incidence angles of the Ar^+ ions set to follow a diverse distribution. These ion energy and dose conditions were selected to reflect realistic plasma etching scenarios encountered in GaN device fabrication. The 1000 eV case represents aggressive etching with high DC bias, the 700 eV condition reflects typical RIE processing, and the 300 eV case simulates milder plasma exposure with minimal damage. The doses were chosen to yield damage depths and amorphization levels in the simulation that

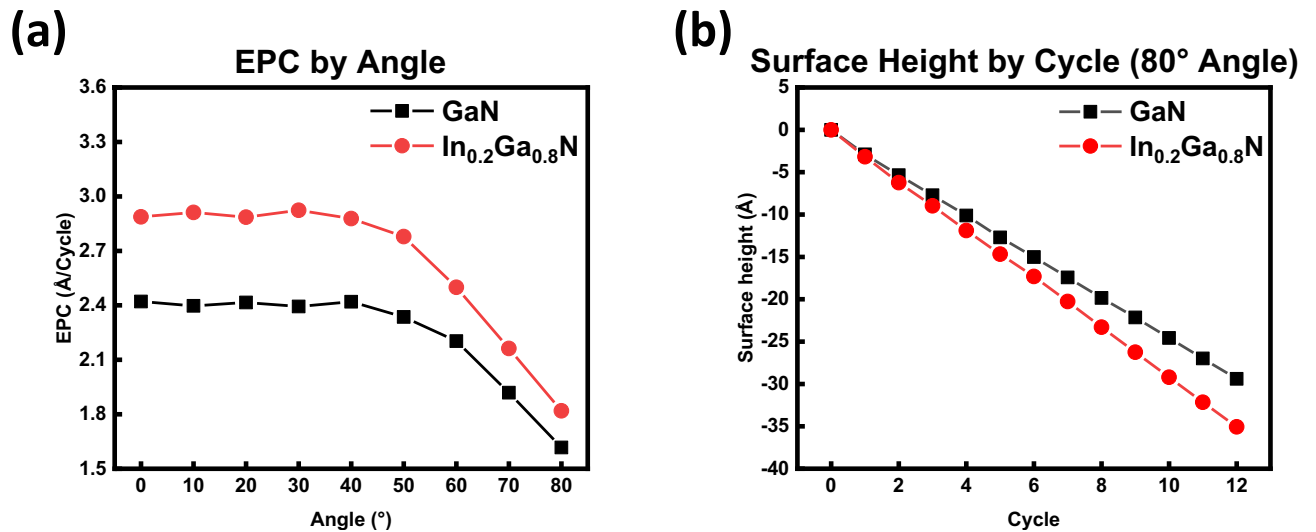


Fig. 3. (a) Angle-dependent EPC and (b) thickness change with etch cycles for GaN and In_{0.2}Ga_{0.8}N at an ion incidence angle of 80°.

Irradiation setup	High damage	Middle damage	Low damage
Ion dose	1.0402e ⁺¹⁶ /cm ²	1.7428e ⁺¹⁵ /cm ²	4.0918e ⁺¹⁵ /cm ²
Ion energy	1000eV	700eV	300eV

Table 1. Information on Ar⁺ ion dose and ion energy irradiated to three types of surfaces for initial damage formation.

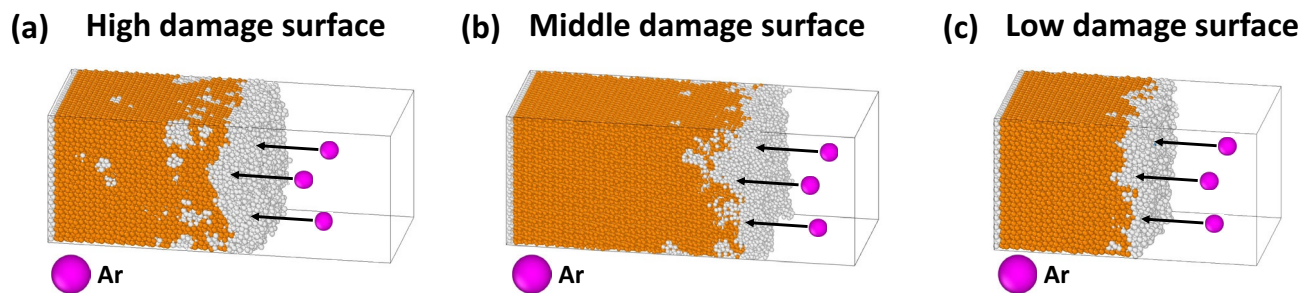


Fig. 4. Structural images of MQW obtained after irradiation of Ar⁺ ion beams from the conditions in Table 1. (a) High damage, (b) Middle damage, and (c) Low damage.

align with experimental observations, thus enabling a systematic study of ALE-based damage recovery across a realistic damage spectrum. Figure 4 (a~c) shows the corresponding structural images for MQW.

The ALE process was applied to the three types of damaged surfaces to simulate the etching and damage recovery behavior. While the ideal ALE aims to precisely remove only a single atomic layer from the surface without causing any damage, in practical simulations such as this one where physical collision with Ar⁺ ions are involved, some degree of damage on surface and subsurface is inevitable. Since the primary objective of this study is to analyze etch-induced damage in MQW structures and explore the potential for damage recovery through ALE, it was necessary to use conditions that more closely resemble actual processing, rather than perfectly idealized scenarios. The Ar⁺ ion dose employed in this simulation was intentionally set slightly higher than the idealized ALE conditions. This was done to replicate the extent of ion-induced damage typically observed in real plasma processes, such as RIE. A higher ion dose introduces a more realistic level of surface and subsurface amorphization, which is necessary to evaluate the damage recovery behavior and efficiency of the ALE process under practically relevant conditions. This approach allows the simulation to capture both the initiation and progression of structural healing across different damage levels.

A single ALE cycle consists of two steps: chemisorption and desorption. A time step of 0.5 fs was used throughout all simulation steps to ensure numerical stability, and unless otherwise specified, all simulations were performed under the NVE ensemble. In the chemisorption step, as shown in Figure 5 (a), 1,600 Cl atoms were

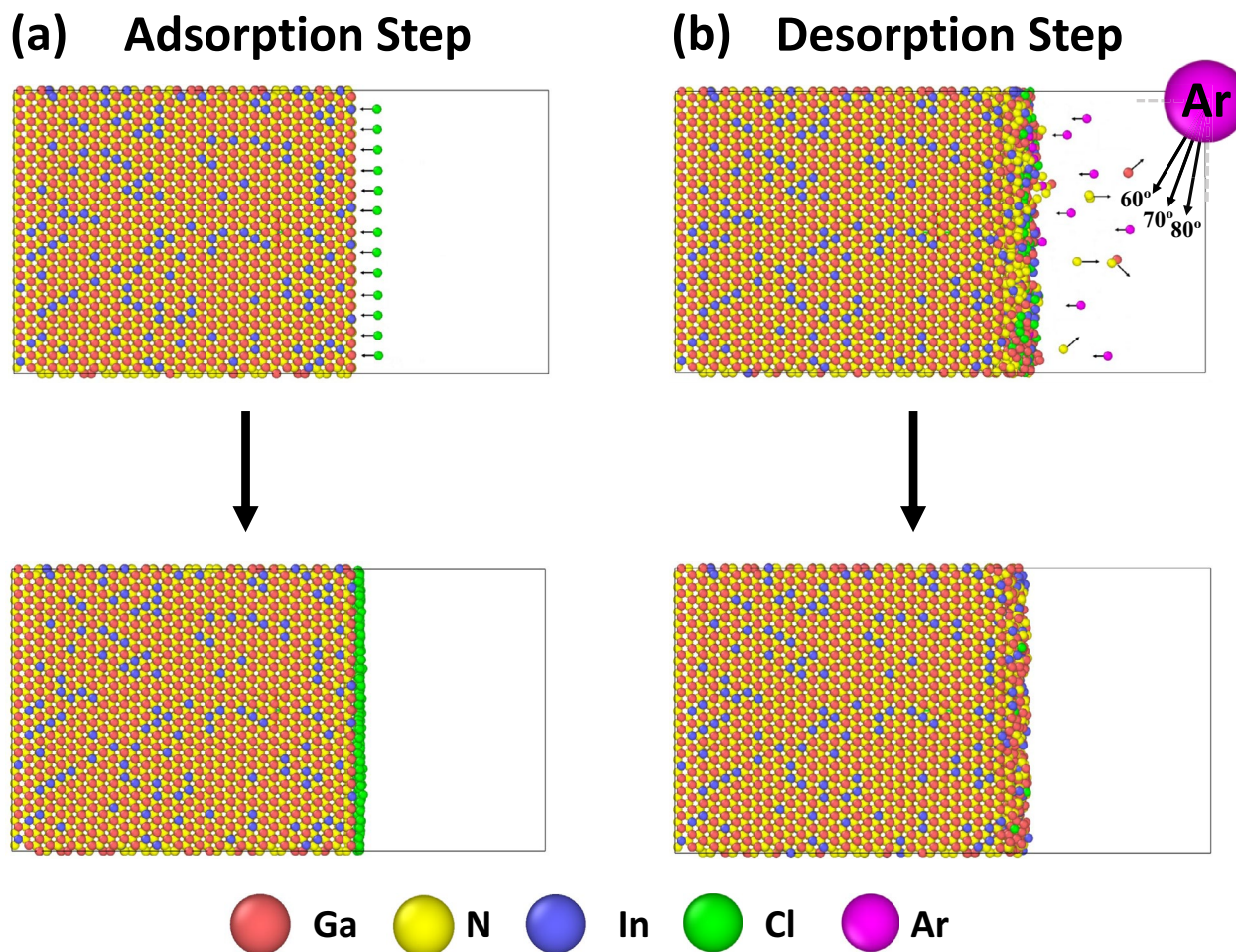


Fig. 5. Side view images from molecular dynamics simulations showing (a) the surface before and after Cl adsorption and (b) before and after Ar desorption for MQW.

randomly introduced onto the surface over a duration of 7.5 ps at a velocity of 0.1 Å/ps, directed perpendicularly to the surface (along the Y-axis). During this process, the substrate temperature was maintained at 300°K using a thermal control layer with Langevin thermostat. This step resulted in the formation of a self-limiting chlorine monolayer. During the desorption step, as shown in Figure 5 (b), an Ar⁺ ion beam with a kinetic energy of 50 eV was irradiated. The Ar⁺ ion beam was simulated by generating ions randomly 10 Å above the surface and then directing them towards it, with their initial velocity components in the y and z directions converted to match the given energy and ion incidence angle. To prevent an abrupt rise in surface temperature and unrealistic dynamics, the total Ar⁺ ion dose was divided into seven sub-cycles and introduced sequentially. Each sub-cycle consisted of a 1.5ps collision process, during which 50 Ar⁺ ions (for a total of 350 ions) were introduced, followed by a 1.1 ps intermediate stabilization and cooling period. During this intermediate stabilization, isolated atoms or byproducts far from the surface (e.g., GaCl₃, N₂) were periodically removed, and a Langevin thermostat was applied to the thermostat layer to cool the system to 300 °K. After all seven sub-cycles were completed, a final stabilization step was performed. This involved removing the main thermal energy for 1.1 ps with the Langevin thermostat, followed by using a Berendsen thermostat to gently bring the system to a smooth convergence at 300 °K. A single ALE cycle, which includes the chemical adsorption (7.5 ps) and desorption (19.3 ps) steps, had a total duration of 26.8 ps and was repeated until the substrate was sufficiently etched.

Analysis methods

For the qualitative analysis and three-dimensional visualization of the simulation results, Open Visualization Tool (OVITO) was employed. For quantitative analysis, the EPC was calculated from the change in the average surface height before and after each cycle, while the surface roughness was quantified by the root-mean-square (RMS) deviation of the y-coordinates of the surface atoms. Crystal damage induced by Ar⁺ ion collisions was analyzed using the Dislocation Analysis (DXA) method, through which the number and distribution of amorphized atoms as well as the depth of the damaged layer were evaluated.

Results and discussion

Figure 6 (a) shows the variation in atomic density with depth during Cl adsorption and desorption on GaN with the methods shown in II-3. During the adsorption, a Cl peak appears near the surface, and although Cl is largely removed after the desorption, a small residual amount remains. This clearly demonstrates that the Cl monolayer is self-limiting during the adsorption and subsequently removed in the desorption process. The distributions of Ga and N remain largely unchanged after the desorption, except for slight variations near the surface region (0~0.5 nm), which indicates the removal of a small number of surface atoms during the ALE process. Figure 6 (c) presents the atomic density variation with depth for $\text{In}_{0.2}\text{Ga}_{0.8}\text{N}$ during Cl adsorption and desorption. Like GaN, the Cl monolayer was self-limiting during the adsorption and removed during the desorption, while the atomic composition remained essentially unchanged after the desorption.

Figure 6 demonstrates that the Cl monolayer is self-limiting during the adsorption and subsequently removed during the desorption process, while the bulk compositions of GaN and $\text{In}_{0.2}\text{Ga}_{0.8}\text{N}$ layers remain essentially unchanged after the desorption. These behaviors along with the observed trends in surface smoothness recovery and damage depth reduction mirror those seen in experimental ALE studies. This qualitative agreement reinforces the accuracy and relevance of the simulation model beyond EPC alone. Atomic densities were calculated by dividing the structure into 2 Å depth intervals along the y-axis and counting the number of atoms per species in each bin. Since the interlayer spacing of Ga-N (or In-Ga-N) is comparable to or smaller than the bin size, atoms from adjacent atomic planes are grouped into the same bin, though minor discrepancies in atom counts may occur if atoms positioned near the bin boundaries cross over due to thermal vibrations. While these results confirm the distinct etch behaviors of each material when considered separately, the situation changes notably in the case of a MQW structure. In our molecular dynamics simulations, we initially calibrated etch parameters to match the experimental EPC values for separate $\text{In}_{0.2}\text{Ga}_{0.8}\text{N}$ and GaN layers, which showed distinct etch rates and characteristics. However, when simulating an integrated MQW structure, the differences between the layers,

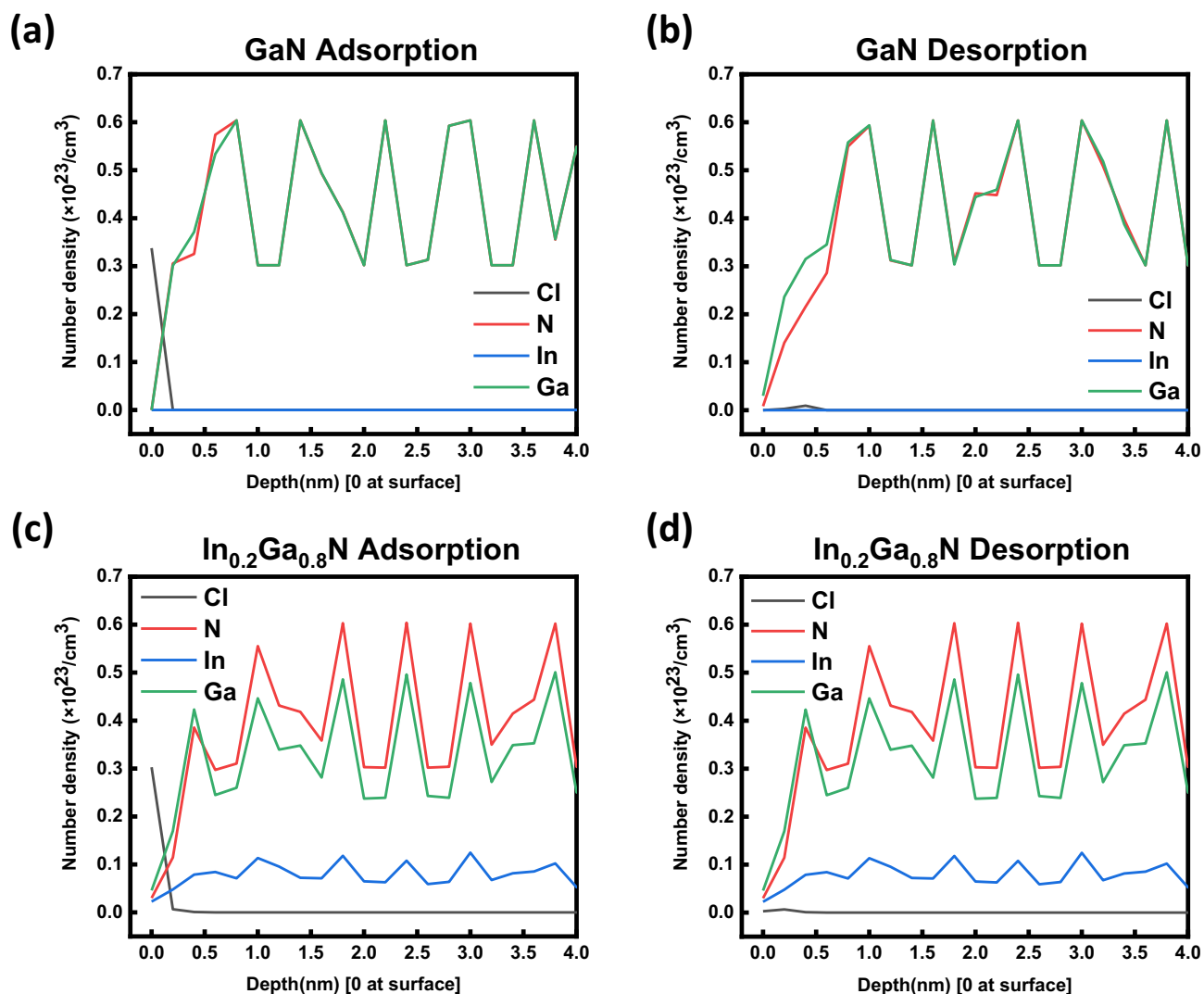


Fig. 6. Atomic density graphs as a function of depth for GaN during (a) adsorption and (b) desorption, and for $\text{In}_{0.2}\text{Ga}_{0.8}\text{N}$ during (c) adsorption and (d) desorption.

not only in their own EPCs but also in other physical properties such as surface roughness and defect generation, became negligible. This discrepancy is attributed to a physically valid phenomenon captured in the simulation: the shallow-angle Ar^+ ion bombardment induces lateral indium migration from the $\text{In}_{0.2}\text{Ga}_{0.8}\text{N}$ layer into the adjacent GaN sidewall. This behavior is driven by two primary mechanisms: (1) lateral momentum transfer due to the oblique ion incidence, and (2) localized thermal spikes that transiently raise atomic mobility near the surface. Although indium atoms are more weakly bound than gallium in the lattice, under such energetic conditions they become more mobile and tend to migrate toward regions of lower potential energy particularly into the slightly damaged but thermally activated GaN layer. Our simulation results show that after several ALE cycles at high ion incidence angles (e.g., 70°), the relative indium concentration at the interface increased by approximately 10–15% compared to the initial distribution, even without additional indium input. This redistribution alters the effective surface composition and leads to more uniform etch characteristics across the multi-layer MQW structure. This result suggests that interfacial atomic migration plays a critical role in damage recovery behavior and must be considered in the process design of anisotropic ALE for heterostructures. This elemental redistribution, driven by a combination of efficient lateral momentum transfer and localized thermal spikes that increase atomic mobility, alters the surface composition at the interface and consequently homogenizes the overall etch behavior and results in similar surface characteristics across the multi-layer stack. These findings highlight that etch characteristics in heterostructures are critically influenced by interfacial atomic migration, a dynamic not observable in single-layer simulations. This phenomenon is further illustrated in Figure 7, which directly visualizes indium migration from the $\text{In}_{0.2}\text{Ga}_{0.8}\text{N}$ layer to the GaN surface under Ar^+ ion bombardment. As a consequence of this indium migration and the resulting surface homogenization, the remainder of the damage recovery analysis considers the MQW sidewall as a unified structure and evaluates the collective changes in its characteristics.

Figure 8 (a–c) show the variation of RMS surface roughness as ALE damage recovery for high, middle, and low damage cases, respectively, for the MQW structure. In the case of high damage, the RMS surface roughness was initially large, but the damage was mitigated after approximately ~45 ALE cycles. Moreover, higher ion incidence angles required a greater number of cycles for recovery. In the middle-damage case, the initial RMS was lower than that of the high-damage case, and the damage was similarly recovered after about ~25 cycles, again with slower recovery observed at higher angles. In the low-damage case, the recovery was achieved after approximately ~15 cycles, and the final RMS values were comparable across all three cases. Figure 8 (d–f) shows the high, middle, and low damage models after damage recovery at an ion incidence angle of 80° , respectively. In the case of low damage, recovery required the fewest cycles, and therefore the largest portion of the structure remained. Notably, the final RMS surface roughness exhibited a clear angular dependence, with the smallest values observed at 80° , gradually increasing as the angle decreased toward 60° . To provide a clear summary of this trend, Table 2 has been added below. It outlines the optimal process window for each ion incidence angle based on recovery efficiency, surface quality, and etching behavior. Furthermore, the final RMS surface roughness values after the recovery became comparable across all cases. Analysis of RMS surface roughness variation as the ALE recovery of single-layer GaN and $\text{In}_{0.2}\text{Ga}_{0.8}\text{N}$ revealed that $\text{In}_{0.2}\text{Ga}_{0.8}\text{N}$ underwent recovery over a more number of cycles than GaN. (See the supplementary information Figure S3)

Figure 9 (a–c) shows damage depth recovery with ALE cycles for high, middle, and low damage cases, respectively for MQW structure. In the case of high damage, higher ion incidence angles required more cycles for recovery, with approximately ~45 cycles needed at 80° . For the middle-damage case, recovery was achieved in

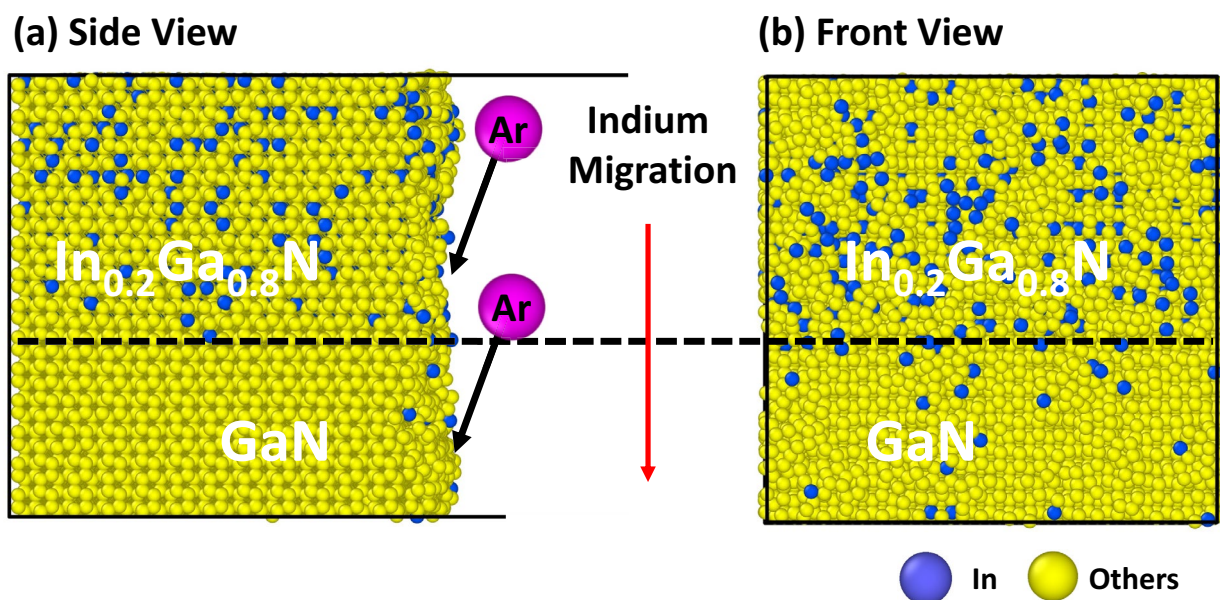


Fig. 7. Visualization of indium migration from the $\text{In}_{0.2}\text{Ga}_{0.8}\text{N}$ layer into the GaN surface under Ar^+ ion bombardment: (a) side view and (b) front view

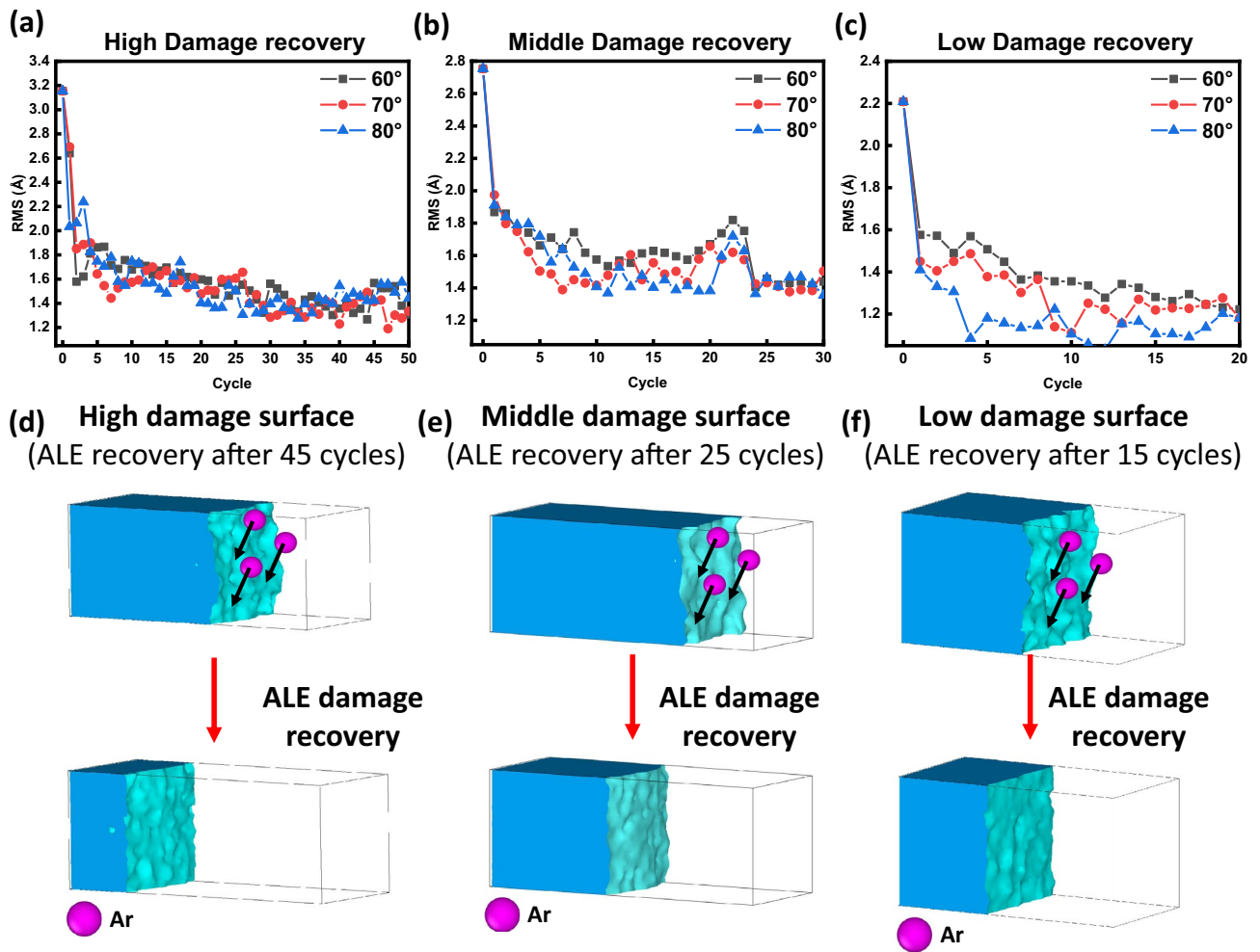


Fig. 8. Ion incidence angle data of damage recovery by ALE cycle for (a) high damage, (b) middle damage, and (c) low damage for MQW structure. Simulation models of ALE damage recovery for MQW structure (at an ion incidence angle of 80°) are shown for (d) high damage, (e) middle damage, and (f) low damage.

Ion incidence angle (°)	Damage recovery efficiency	Surface roughness	Etch depth control	Recommended usage
60°	High (rapid damage removal)	Higher (rougher surface)	Deeper material removal	Initial cycles for bulk damage removal
70°	Moderate	Balanced	Moderate control	Intermediate phase in ALE
80°	Slower recovery	Lowest (smoothest surface)	Shallow, precise etching	Final phase for surface refinement

Table 2. Summary of optimal ALE process conditions as a function of ion incidence angle. The table compares damage recovery efficiency, surface roughness, etch depth behavior, and the recommended usage in multi-step atomic layer etching strategies for GaN-based MQW structures.

about ~25 cycles, while in the low-damage case, full recovery occurred within ~15 cycles. Despite the differences in required cycles, the final residual damage depth values converged to similar levels, demonstrating that ALE can effectively recover damage across different initial conditions. Figure 9 (d~f) shows the structural evolution at representative ALE cycles for high, middle, and low damage cases at an ion incidence angle of 80°. In the high-damage case, a larger ion dose and more cycles were required for recovery, resulting in a greater material removal and thus a thinner remaining surface layer. Conversely, the low-damage case required fewer cycles for full recovery. Despite these differences, the final residual damage depths converged to similar levels across all cases, confirming the effective recovery capability of ALE. This can be attributed to the relatively small variation in incidence angles (60°–80°) and the low Ar⁺ ion energy (~50 eV), which together limit the angular dependence of damage formation. However, when the range of incidence angles was further extended to include near-normal incidence, the difference in residual damage depth became more pronounced, indicating that the angular dependence of surface damage increases significantly under such conditions. (See the supplementary

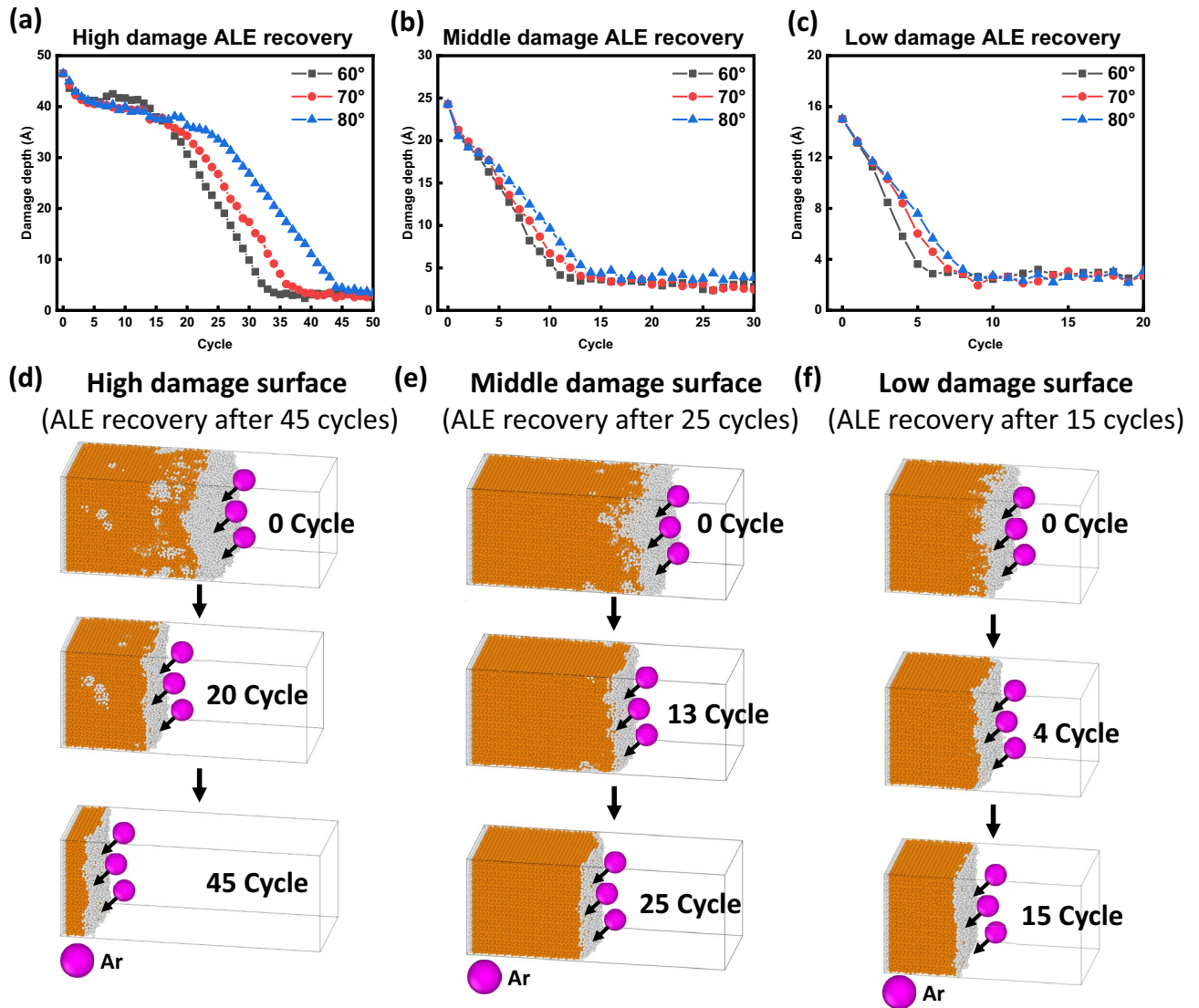


Fig. 9. Recovery of damage depth with ALE cycles for MQW structure: (a) high damage, (b) middle damage, and (c) low damage. MD simulation models of damage recovery at an ion incidence angle of 80° for MQW structure: (d) high damage, (e) middle damage, and (f) low damage.

information Figure S4) A comparison between GaN and $\text{In}_{0.2}\text{Ga}_{0.8}\text{N}$ revealed that $\text{In}_{0.2}\text{Ga}_{0.8}\text{N}$ recovered its damage depth over a more number of cycles than GaN. (See the supplementary information Figure S4)

To evaluate the recovery of amorphized regions as an additional damage recovery method, Figure 10 (a–c) show simulations performed for high, middle, and low damage conditions at ion incidence angles of 60° ~ 80°, respectively. In all three cases, the damage was eventually removed after sufficient ALE cycles. However, the percentage of damage removal decreased from the high damage to the low damage case. This indicates that surfaces with greater initial damage require a larger number of ALE recovery cycles but ultimately achieve the highest removal percentage, whereas less damaged surfaces recover more quickly but with a lower removal percentage. Furthermore, the final residual amorphous atoms values converged to similar levels across all conditions, suggesting that ALE can effectively restore crystallinity regardless of the initial damage level, provided that the Ar^+ ion energy used in the ALE process is sufficiently low (~50 eV) to minimize physical damage to the lattice atoms, although the recovery dynamics vary depending on the extent of damage. When examining each material, $\text{In}_{0.2}\text{Ga}_{0.8}\text{N}$ and GaN, the results are consistent with the trends observed in Figure 10, confirming that the ALE process effectively removes amorphous regions regardless of the initial damage level. (See the supplementary information Figure S5)

Conclusions

This study employed molecular dynamics (MD) simulations to identify the optimal conditions of the ALE process for damage recovery on the sidewalls of GaN-based devices. In particular, the effect of ion incidence angle on the damage recovery of ($\text{In}_{0.2}\text{Ga}_{0.8}\text{N}/\text{GaN}$) multiple quantum well (MQW) structures was systematically analyzed

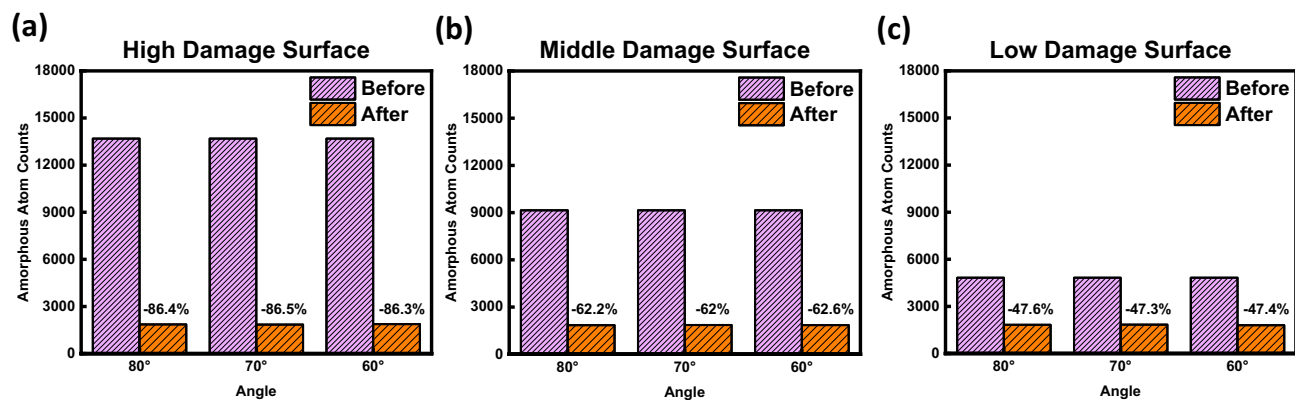


Fig. 10. Differences in the recovery of amorphized regions before and after damage recovery by the ALE process for (a) high damage, (b) middle damage, and (c) low damage in the MQW structure. The number of ALE cycles used to achieve sufficient recovery was approximately ~45 cycles for high damage, ~25 cycles for middle damage, and ~15 cycles for low damage, respectively.

at the atomic scale. The simulation results revealed that the ALE process effectively removes both surface and subsurface damaged regions induced by RIE. For all three types of initially damaged surfaces (high, middle, and low damage), ALE consistently reduced amorphized atoms by over ~47%, ultimately leaving a similar level of residual surface damage across cases. This indicates that ALE possesses strong potential to fundamentally recover damaged regions regardless of the initial extent of damage. Furthermore, the ion incidence angle was found to be a key parameter in determining the efficiency of ALE-based damage recovery. When the ion beam approaches normal incidence, the EPC increases, which facilitates faster removal of damaged layers. Based on these characteristics, we propose a two-step strategy: initially utilizing 60°–70° for bulk damage removal, and subsequently switching to a shallower angle of 80° to minimize surface roughness. Although the dynamic transition was not explicitly simulated, this strategy is derived from the complementary benefits observed at each fixed angle. This stepwise approach reflects a practical process scenario where the substrate tilt is mechanically controlled in ion beam systems. Consequently, this dual-angle concept is expected to improve the balance between etch efficiency and surface smoothing, minimizing both damage depth and roughness effectively. More comprehensive strategy comparisons, including the dynamic effects of angle transition, are suggested as subjects for future investigation. The results shown in Figures 8 and 9 provide a comparative perspective among individual fixed angles (60°, 70°, 80°). These results demonstrate that lower angles accelerate damage removal but yield rougher surfaces, while 80° results in the smoothest finish with slower removal. Therefore, the proposed two-step strategy was derived by combining the complementary benefits of each angle. This rationale has been clarified in the text, and more comprehensive strategy comparisons are suggested as a subject for future investigation. This strategy was shown to be the most effective. Therefore, to create vertical, damage-free GaN-based devices, it is suggested that an ion beam ALE system with a tilting substrate would be effective after RIE and wet etching. Finally, by demonstrating the utility of molecular dynamics simulations in designing and optimizing processes at the atomic level, this work provides both critical physical insights and practical guidelines for advancing semiconductor and display processing technologies.

Data availability

Data will be made available on request to Geun Young Yeom. (gyyeom@skku.edu).

Received: 13 October 2025; Accepted: 29 January 2026

Published online: 03 February 2026

References

- Hwang, D., Mughal, A., Pynn, C. D., Nakamura, S. & DenBaars, S. P. Sustained high external quantum efficiency in ultrasmall blue III-nitride micro-LEDs. *Appl. Phys. Express* <https://doi.org/10.7567/APEX.10.032101> (2017).
- Liu, Z. et al. Advanced technologies in InGaN micro-LED fabrication to mitigate the sidewall effect. *Light Sci. Appl.* <https://doi.org/10.1038/s41377-025-01751-y> (2025).
- Huang, Y., Hsiang, E. L., Deng, M. Y. & Wu, S. T. Mini-LED Micro-LED and OLED displays: present status and future perspectives. *Light Sci. Appl.* <https://doi.org/10.1038/s41377-020-0341-9> (2020).
- Debnath, R. et al. Top-down fabrication of large-area GaN micro- and nanopillars. *J. Vac. Sci. Technol. B Nanotechnol. Microelectron.: Mater. Process. Meas. Phenomena* **10**(1116/1), 4865908 (2014).
- Deshpande, G., Bhattacharya, S., Ajayan, J., Mounika, B. & Nirmal, D. A review of GaN channel-based MOSHEMTs for next-generation medium/low-voltage rating and high-speed rf power applications. *J. Electron. Mater.* **53**, 4287–4307. <https://doi.org/10.1007/s11664-024-11177-8> (2024).
- Ding, K., Avrutin, V., Izyumskaya, N., Özgür, Ü. & Morkoç, H. Micro-LEDs, a manufacturability perspective. *Appl. Sci. (Switzerland)* <https://doi.org/10.3390/app9061206> (2019).
- Chen, P. W. et al. On the mechanism of carrier recombination in downsized blue micro-LEDs. *Sci. Rep.* <https://doi.org/10.1038/s41598-021-02293-0> (2021).

8. Yang, T. Y. et al. A normally-Off GaN MIS-HEMT fabricated using atomic layer etching to improve device performance uniformity for high power applications. *IEEE Electron. Device Lett.* **43**, 1629–1632. <https://doi.org/10.1109/LED.2022.3201900> (2022).
9. Liu, A. C. et al. Improving performance and breakdown voltage in normally-off GaN recessed gate MIS-HEMTs using atomic layer etching and gate field plate for high-power device applications. *Micromachines (Basel)* <https://doi.org/10.3390/mi14081582> (2023).
10. Ruel, S. et al. Atomic layer etching of GaN using Cl₂ and He or Ar plasma. *J. Vacuum Sci. Technol. A: Vacuum Surf. Films* <https://doi.org/10.1116/6.0000830> (2021).
11. Pearton, S. J., Shul, R. J. & Ren, F. A review of dry etching of GaN and related materials. *MRS Internet J. Nitride Semicond. Res.* **5**, 11 (2000). <https://doi.org/10.1557/S1092578300000119>
12. He, K. et al. Surface properties of indium tin oxide treated by Cl₂ inductively coupled plasma. *Appl. Surf. Sci.* **316**, 214–221. <https://doi.org/10.1016/j.apsusc.2014.08.016> (2014).
13. Sun, Y. et al. Optimization of mesa etch for a quasi-vertical gan schottky barrier diode (Sbd) by inductively coupled plasma (icp) and device characteristics. *Nanomaterials* <https://doi.org/10.3390/nano10040657> (2020).
14. Liu, Z. et al. Fabrication of GaN hexagonal cones by inductively coupled plasma reactive ion etching. *J. Vacuum Sci. Technol. B Nanotechnol. Microelectron.: Mater. Process. Meas. Phenom.* <https://doi.org/10.1116/1.4954986> (2016).
15. Ladroue, J. et al. Deep GaN etching by inductively coupled plasma and induced surface defects. *J. Vac. Sci. Technol. A: Vac. Surf. Films* **28**, 1226–1233. <https://doi.org/10.1116/1.3478674> (2010).
16. Wang, K. et al. Pulsed N₂ plasma surface treatment for AlGaIn/GaN HEMTs prior to PECVD SiNx passivation to reduce plasma damage. *Appl. Phys. Lett.* <https://doi.org/10.1063/5.0235740> (2024).
17. Li, Q. et al. Efficient access to non-damaging GaN (0001) by inductively coupled plasma etching and chemical–mechanical polishing. *Appl. Surf. Sci.* <https://doi.org/10.1016/j.apsusc.2024.161207> (2025).
18. Mohanta, A. et al. Observation of weak carrier localization in green emitting InGaIn/GaN multi-quantum well structure. *J. Appl. Phys.* <https://doi.org/10.1063/1.4917217> (2015).
19. Najjar, A., Shafa, M. & Anjum, D. Synthesis, optical properties and residual strain effect of GaN nanowires generated: via metal-assisted photochemical electroless etching. *RSC Adv.* **7**, 21697–21702. <https://doi.org/10.1039/c7ra02348k> (2017).
20. Paramanik, D., Motayed, A., King, M., Ha, J.-Y., Kryluk, S., Davydov, A. V. & Talin, A. Fabrication of high quality GaN nanopillar arrays by dry and wet chemical etching. arXiv preprint arXiv:1311.0321v3 (2013). <https://arxiv.org/abs/1311.0321>
21. Jaloustre, L., Sales De Mello, S., Labau, S., Petit-Etienne, C. & Pargon, E. Faceting mechanisms of GaN nanopillar under KOH wet etching. *Mater. Sci. Semicond. Process* <https://doi.org/10.1016/j.mssp.2023.108095> (2024).
22. Lee, J.-M., Lee, K.-S. & Park, S.-J. Removal of dry etch damage in p-type GaN by wet etching of sacrificial oxide layer. *J. Vacuum Sci. Technol. B: Microelectron. Nanometer Struct. Process. Meas. Phenom.* **22**, 479–482. <https://doi.org/10.1116/1.1645880> (2004).
23. Kanarik, K. J. et al. Overview of atomic layer etching in the semiconductor industry. *J. Vacuum Sci. Technol. A: Vacuum Surf. Films* <https://doi.org/10.1116/1.4913379> (2015).
24. Vella, J. R. & Graves, D. B. Near-surface damage and mixing in Si-Cl₂-Ar atomic layer etching processes: Insights from molecular dynamics simulations. *J. Vacuum Sci. Technol. A* <https://doi.org/10.1116/6.0002719> (2023).
25. Guan, L., Li, X., Che, D., Xu, K. & Zhuang, S. Plasma atomic layer etching of GaN/AlGaIn materials and application: an overview. *J. Semicond.* <https://doi.org/10.1088/1674-4926/43/11/113101> (2022).
26. Kauppinen, C. et al. Atomic layer etching of gallium nitride (0001). *J. Vacuum Sci. Technol. A: Vacuum Surf. Films* <https://doi.org/10.1116/1.4993996> (2017).
27. K. Nojiri, T. Ohba, K.J. Kanarik, Atomic layer etching of GaN and AlGaIn using directional plasma-enhanced approach <https://www.researchgate.net/publication/328418893> (2018).
28. Kim, D. S. et al. Atomic layer etching of Sn by surface modification with H and Cl radicals. *Nanotechnology* <https://doi.org/10.1088/1361-6528/ac9981> (2023).
29. Ohba, T., Yang, W., Tan, S., Kanarik, K. J. & Nojiri, K. Atomic layer etching of GaN and AlGaIn using directional plasma-enhanced approach. *Jpn. J. Appl. Phys.* <https://doi.org/10.7567/JJAP.56.06HB06> (2017).
30. Fischer, A., Routzahn, A., George, S. M. & Lill, T. Thermal atomic layer etching: a review. *J. Vacuum Sci. Technol. A: Vacuum Surf. Films* <https://doi.org/10.1116/6.0000894> (2021).
31. Kim, C. H. et al. Effect of atomic layer etching on the surface damage removal of GaN-based light emitting diodes. *Appl. Surf. Sci.* <https://doi.org/10.1016/j.apsusc.2025.164429> (2025).
32. Park, J. W. et al. Atomic layer etching of InGaAs by controlled ion beam. *J. Phys. D Appl. Phys.* <https://doi.org/10.1088/1361-6463/aa70c8> (2017).
33. Park, J. W., Kim, D. S., Lee, W. O., Kim, J. E. & Yeom, G. Y. Atomic layer etching of chrome using ion beams. *Nanotechnology* <https://doi.org/10.1088/1361-6528/aaf521> (2019).
34. Vella, J. R., Hao, Q., Donnelly, V. M. & Graves, D. B. Dynamics of plasma atomic layer etching: molecular dynamics simulations and optical emission spectroscopy. *J. Vacuum Sci. Technol. A* <https://doi.org/10.1116/6.0003011> (2023).
35. Vella, J. R., Humbird, D. & Graves, D. B. Molecular dynamics study of silicon atomic layer etching by chlorine gas and argon ions. *J. Vacuum Sci. Technol. B* <https://doi.org/10.1116/6.0001681> (2022).
36. Gruber, J., Zhou, X. W., Jones, R. E., Lee, S. R. & Tucker, G. J. Molecular dynamics studies of defect formation during heteroepitaxial growth of InGaIn alloys on (0001) GaN surfaces. *J. Appl. Phys.* <https://doi.org/10.1063/1.4983066> (2017).
37. Fu, W. Y. & Choi, H. W. Phosphor-free InGaIn nanopillar white LEDs by random clustering of mono-sized nanospheres. *Appl. Phys. Lett.* **118**, 201106 (2021). <https://doi.org/10.1063/5.0049629>
38. Chen, C. et al. Vacancy-assisted core transformation and mobility modulation of a-type edge dislocations in wurtzite GaN. *J. Phys. D Appl. Phys.* <https://doi.org/10.1088/1361-6463/ab3f78> (2019).
39. Fu, W. Y. & Choi, H. W. Explaining relative spectral red shifts in InGaIn/GaN micropillars. *Optica* **5**, 765. <https://doi.org/10.1364/optica.5.000765> (2018).
40. Zhou, X. W., Jones, R. E. & Chu, K. Polymorphic improvement of Stillinger-Weber potential for InGaIn. *J. Appl. Phys.* <https://doi.org/10.1063/1.5001339> (2017).
41. Wang, Z., Zu, X., Gao, F. & Weber, W. J. Atomic-level study of melting behavior of GaN nanotubes. *J. Appl. Phys.* <https://doi.org/10.1063/1.2345616> (2006).
42. Zhou, X. W. & Jones, R. E. A Stillinger-Weber potential for InGaIn. *J. Mater. Sci. Res.* **6**, 88–95 (2017). <https://doi.org/10.5539/jms.r.v6n4p88>
43. Shulga, V. I. & Sigmund, P. Analysis of the primary process in isotope sputtering. *Nucl. Instrum. Methods Phys. Res. Sect. B: Beam Interact. Mater. Atoms* **119**(3), 359–374 (1996).
44. Robinson, M. T. & Torrens, L. M. Computer simulation of atomic-displacement cascades in solids in the binary-collision approximation. *Phys. Rev. B* **9**, 5008–5024 (1974). <https://doi.org/10.1103/PhysRevB.9.5008>
45. Lenhard, J., Stephan, S. & Hasse, H. On the history of the Lennard-Jones potential. *Ann. Phys.* <https://doi.org/10.1002/andp.202401115> (2024).
46. Pieprzyk, S., Brańka, A. C., MacKowiak, S. & Heyes, D. M. Comprehensive representation of the Lennard-Jones equation of state based on molecular dynamics simulation data. *J. Chem. Phys.* <https://doi.org/10.1063/1.5021560> (2018).
47. Toghraie Semiro, D. & Azimian, A. R. Molecular dynamics simulation of annular flow boiling with the modified Lennard-Jones potential function. *Heat Mass Transfer/Waerme- Und Stoffuebertragung* **48**, 141–152. <https://doi.org/10.1007/s00231-011-0855-z> (2012).

48. H. Sun, COMPASS: An ab initio force-field optimized for condensed-phase applications overview with details on alkane and benzene compounds <https://pubs.acs.org/sharingguidelines> (1998).

Acknowledgments

This work was supported by the Korea Institute of Energy Technology Evaluation and Planning (KETEP) and the Ministry of Trade, Industry & Energy (MOTIE) of the Republic of Korea (No. RS-2022-KP002701).

Author contributions

E.K.K and J.W.H contributed to the experimental design. W.S.L contributed to the experimental setup. J.Y.K, K.L.K, J.S.P and Y.J.P contributed to the data analysis. C.H.K and H.J.E, J.W.J, S.H.K, Y.W.J initiated the project. G.Y.Y and D.W.K participated in writing the manuscript.

Declarations

Competing interests

The authors declare that they have no known competing financial interests or personal relationships that could have appeared to influence the work reported in this paper. The authors declare no competing interests.

Additional information

Supplementary Information The online version contains supplementary material available at <https://doi.org/10.1038/s41598-026-38333-w>.

Correspondence and requests for materials should be addressed to G.Y.Y.

Reprints and permissions information is available at www.nature.com/reprints.

Publisher's note Springer Nature remains neutral with regard to jurisdictional claims in published maps and institutional affiliations.

Open Access This article is licensed under a Creative Commons Attribution-NonCommercial-NoDerivatives 4.0 International License, which permits any non-commercial use, sharing, distribution and reproduction in any medium or format, as long as you give appropriate credit to the original author(s) and the source, provide a link to the Creative Commons licence, and indicate if you modified the licensed material. You do not have permission under this licence to share adapted material derived from this article or parts of it. The images or other third party material in this article are included in the article's Creative Commons licence, unless indicated otherwise in a credit line to the material. If material is not included in the article's Creative Commons licence and your intended use is not permitted by statutory regulation or exceeds the permitted use, you will need to obtain permission directly from the copyright holder. To view a copy of this licence, visit <http://creativecommons.org/licenses/by-nc-nd/4.0/>.

© The Author(s) 2026